








Vernier effect-based tunable mid-infrared sensor using silicon-on-insulator cascaded rings

YUHUA CHANG,^{1,2}  BOWEI DONG,^{1,2}  YIMING MA,^{1,2}  JINGXUAN WEI,^{1,2}  ZHILAO REN,^{1,2} AND CHENGKUO LEE^{1,2,*} 

¹Department of Electrical and Computer Engineering, National University of Singapore, 117583, Singapore

²Center for Intelligent Sensors and MEMS, National University of Singapore, 117608, Singapore

*elelc@nus.edu.sg

Abstract: Vernier effect has been captivated as a promising approach to achieve high-performance photonic sensors. However, experimental demonstration of such sensors in mid-infrared (MIR) range, which covers abundant absorption fingerprints of molecules, is still lacking. Here, we report Vernier effect-based thermally tunable photonic sensors using cascaded ring resonators fabricated on the silicon-on-insulator (SOI) platform. The radii and the coupling gaps in two rings are investigated as key design parameters. By applying organic liquids on our device, we observe an envelope shift of 48 nm with a sensitivity of 3000 nm/RIU and an intensity drop of 6.7 dB. Besides, our device can be thermally tuned with a sensitivity of 0.091 nm/mW. Leveraging the characteristic molecular absorption in the MIR, our work offers new possibilities for complex index sensing, which has wide applications in on-chip photonic sensors.

© 2020 Optical Society of America under the terms of the [OSA Open Access Publishing Agreement](#)

1. Introduction

Photonic sensors have garnered extensive research attention over the past decades. In the early development stage of photonic sensors, most of them are based on the refractometric sensing mechanism [1]. Through interacting with the evanescent wave, the change of refractive index in the surrounding environment influences the effective index of the propagating mode in the photonic waveguide. Consequently, the resonant wavelength shifts. Ring resonators [2], surface plasmon resonance [3], Bragg gratings [4] and photonic crystal [5–9] have been investigated. Among them, cascaded resonators using Vernier effect show ultrahigh sensitivity because the resonant shift from a single resonator is amplified by the difference in free spectrum ranges (FSR) between two resonators [10]. Significant efforts have been devoted to further boosting the sensing performances. Three cascaded ring resonators [11] and a Mach–Zehnder interferometer (MZI) cascaded with the ring resonator [12] were experimentally demonstrated for ultrahigh sensitivity and larger measurement range respectively. Partially suspended waveguides [13] and transverse-magnetic mode waveguides [14] were also employed to enhance the light-matter interaction. A sensitivity as high as 24,300 nm/RIU (refractive index unit) [14] has been achieved and an ultralow limit of detection (LOD) reaches 10^{-6} RIU [13,15]. However, the refractometric sensing lacks selectivity and requires further surface functionalization [16].

Besides the refractometric sensor, the other category of photonic sensors is based on the absorption sensing mechanism [17]. The mid-infrared (MIR) range is an ideal working window for the absorption-based photonic sensors because it covers the molecular fingerprints of many chemical and biological species in their gaseous or liquid forms [18–22]. As the light propagates in the photonic waveguide, the intensity is attenuated at specific wavelengths due to the absorption caused by the interaction between the molecular fingerprints and the evanescent wave. Therefore, the selective discrimination of chemical bonds is realized by observing the wavelength where light is absorbed. On top of the development of fundamental MIR building blocks [23–27], various waveguide structures have been investigated to enhance the absorption from the analytes, such as directional coupler [28], pedestal waveguide [29], slot waveguide [30], photonic crystal

waveguide [31] and spiral waveguide [32]. However, only the extinction coefficient k can be obtained by waveguide structures. To simultaneously leverage the high sensitivity offered by refractometric sensing and the selectivity offered by absorption sensing, the Vernier effect-based MIR photonic sensor is expected to be a promising candidate. In the previous MIR works, the general design flow and MIR sensing performance were studied theoretically [33]. Cascaded rings were also characterized based on germanium-on-insulator (GeOI) [34], silicon-on-insulator (SOI) [35], Ge-on-SOI [36] and germanium-on-silicon (Ge-on-Si) [37] platforms. Nevertheless, no experimental demonstration of Vernier effect-based MIR sensing has been reported so far. A systematic study is also needed as the design guideline, which correlates the geometric parameters of Vernier structures with its figures of merit. In addition, the thermally tunable Vernier filter on SOI platform is still lacking.

In this work, we design, fabricate and characterize the Vernier effect-based tunable MIR photonic sensor using cascaded rings. The relationship between major figures of merit (FSR_{Vernier} , envelope peak) and two key geometric parameters (ring radius, coupling gap) is investigated as the design guideline. The thermal tunability is also demonstrated. Finally, a microfluidic channel is bonded to the sensor and the detection of organic liquids is realized as a proof-of-concept demonstration of complex index sensing.

2. Device concept, fabrication, and characterization

A typical Vernier spectrum in a single FSR is simulated and presented in Fig. 1(a). Figure 1(b) is the schematic illustration of two cascaded rings with microheaters and cladding SiO_2 openings. Two add-drop ring resonators with minor radii differences are cascaded at the drop ports, with one as a reference ring and the other as a sensing ring. The radii mismatch causes the difference in both peak wavelength and FSR, as indicated by blue and orange curves in Fig. 1(a). For a single ring resonator, the transmitted spectrum at through/drop port and the FSR are described by [38]

$$T_{\text{through}} = \frac{r^2 a^2 - 2r^2 a \cos \phi + r^2}{1 - 2r^2 a \cos \phi + (r^2 a)^2} \quad (1)$$

$$T_{\text{drop}} = \frac{(1 - r^2)^2 a}{1 - 2r^2 a \cos \phi + (r^2 a)^2} \quad (2)$$

$$FSR = \frac{\lambda^2}{n_g L} \quad (3)$$

where a and ϕ are the amplitude and the phase shift of transmitted light after one single-pass respectively. r is the self-coupling coefficient. L is the perimeter of the rings, while n_g is the group index. The overall Vernier spectrum is the product of the spectra at drop ports of two cascaded rings, as indicated by the black curve in Fig. 1(a). In the spectrum, the transmission is highest at the center and gradually decreases on both sides, forming a Vernier envelope. The peak of the spectrum envelope is caused by the perfect matching of two spectra of individual rings. At other wavelengths, the mismatch of individual spectra increases, leading to a reduction in the envelope height. The FSR of the Vernier envelop FSR_{Vernier} is defined in [10].

$$FSR_{\text{Vernier}} = \frac{FSR_{\text{sensor}} FSR_{\text{ref}}}{|FSR_{\text{sensor}} - FSR_{\text{ref}}|} = \frac{\lambda_r^2 \lambda_s^2}{2\pi} \frac{1}{|\lambda_r^2 R_s n_{g,s} - \lambda_s^2 R_r n_{g,r}|} \quad (4)$$

where $\lambda_s(\lambda_r)$, $n_{g,s}(n_{g,r})$ and $R_s(R_r)$ are the center wavelength, group index and radius for sensing(reference) ring respectively. The optical microscope image of the device is shown in Fig. 1(c). The inset is the scanning electron microscope (SEM) image of a 350 nm coupling gap. To fabricate the devices, a 180 nm single-crystal Si layer is grown by epitaxy on the SOI

wafer with a 220 nm device layer and 2 μm buried oxide. Then 400 nm Si is fully etched to define the 1.2 μm wide waveguide. After a 2 μm upper cladding SiO_2 is deposited and polished, the TiN microheater is implemented on top of the reference ring. The devices are characterized by a fiber-based testing setup as sketched in Fig. 1(d). The light from the MIR laser (MIRcat-1200, Daylight Solutions) is modulated by chopper and coupled into a ZrF_4 fiber by a ZnSe lens. It is further coupled into the waveguide through the butt coupling method. The input and output waveguide is tapered to mitigate the mode mismatch for a lower coupling loss. The output is detected by a commercial PbSe detector, which is connected to the lock-in amplifier operating at chopper frequency.

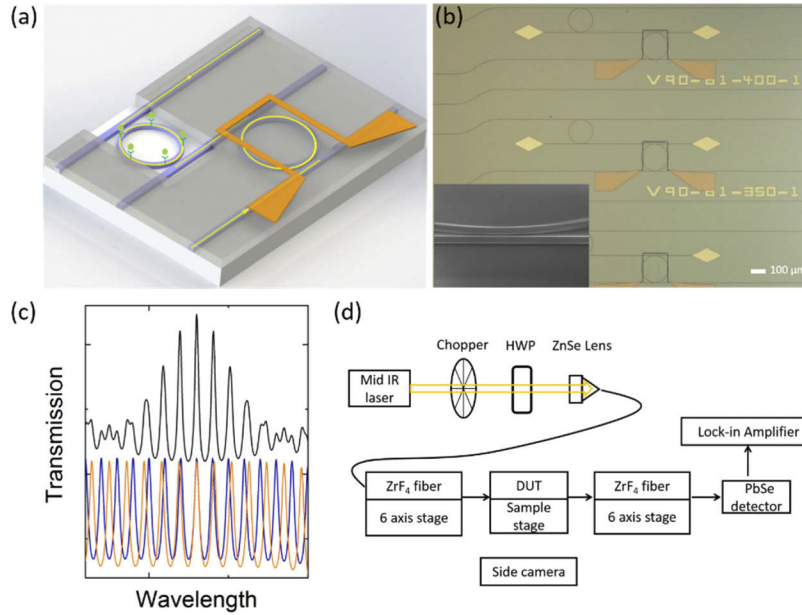


Fig. 1. (a) Simulated spectra of the cascaded rings (black) and two separate rings (blue and orange lines). (b) Schematic illustration of cascaded rings with TiN heater and SiO_2 opening. (c) Optical microscope image of the devices with heater. Inset is the SEM image of the coupling gap. (d) Diagram of the MIR testing setup. HWP: half-wave plate. DUT: device under test.

To experimentally demonstrate the Vernier effect, we characterized two cascaded rings with radii of 90 μm (reference ring) and 81 μm (sensing ring) and a coupling gap of 400 nm. The measured spectrum from 3.64 μm to 4 μm at the through port of the sensing ring is plotted in Fig. 2(a). Figure 2(b) is the zoom-in image of the circled area. The Gaussian fitting indicates a quality factor of around 4000 and an extinction ratio of 10 dB. The individual FSRs of two rings are measured to be 6.1 nm and 6.8 nm respectively. Figure 2(c) is the overall Vernier spectrum where the measured FSR_{Vernier} (61.8 nm) agrees with the theoretical FSR_{Vernier} (59.25 nm). The Vernier gain G is 9.71, which is defined in [10].

$$G = \frac{FSR_{ref}}{|FSR_{sensor} - FSR_{ref}|} = \frac{\frac{\lambda_r^2}{2\pi R_r n_{g,r}}}{\left| \frac{\lambda_r^2}{2\pi R_r n_{g,r}} - \frac{\lambda_s^2}{2\pi R_s n_{g,s}} \right|} = \frac{1}{\left| \frac{\lambda_r^2 R_r n_{g,r}}{\lambda_s^2 R_s n_{g,s}} - 1 \right|} \quad (5)$$

The increasing transmission intensity at longer wavelength is attributed to the coupling condition that is gradually shifted to the over-coupling region. The extinction ratio of the envelope is 23.8 dB at 3.7 μm and is reduced to 14.6 dB at 3.95 μm due to the absorption of cladding SiO_2 .

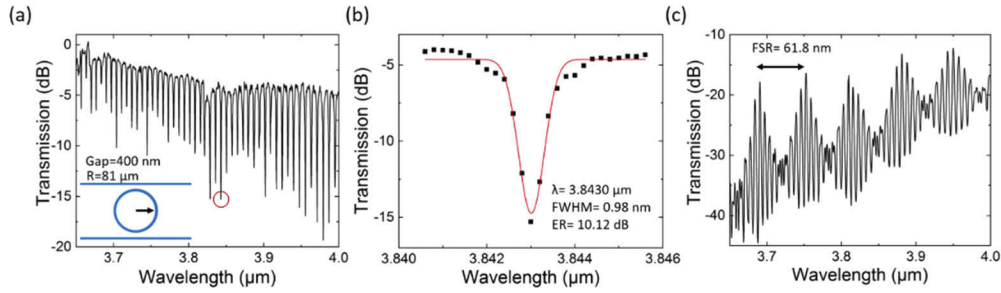


Fig. 2. (a) Normalized spectrum at the through port of the sensing ring. (b) Zoom-in and Gaussian fitting results of the circled single resonance in (a). (c) The overall normalized spectrum of two cascaded rings with radii of 90 μm and 81 μm .

In the cascaded rings, the radii and the coupling gaps are the two key design parameters that determine the major figures of merit: FSR_{Vernier} and envelope peak, which is the wavelength of the highest transmission in the Vernier envelope. To investigate the influence of geometric parameters on FSR_{Vernier} and envelope peak, an array of cascaded rings are systematically designed and fabricated. Firstly, cascaded rings with radii varied from 100/90 μm to 40/36 μm are characterized. Five measured spectra are plotted in Fig. 3(a), where the shaded area indicates the corresponding FSR_{Vernier} . The coupling gap is fixed at 300 nm. The decreasing radii difference broadens the overall Vernier envelope and the FSR of interstitial peaks ($FSR_{\text{interstitial}}$) is increased by the smaller radius. Figure 3(b) depicts the comparison between experimental and theoretical FSR_{Vernier} . Under the condition that both rings are buried under cladding SiO_2 ($\lambda_s = \lambda_r$, $n_{g,s} = n_{g,r}$), the FSR_{Vernier} can be calculated by the Eq. (4),

$$FSR_{\text{Vernier}} = \frac{\lambda^2}{2\pi n_g |\Delta R|} \quad (6)$$

Where the group index n_g is simulated to be 3.99 for TE mode waveguide and λ is the center wavelength. The measured fitting curve shows a good agreement with the theory.

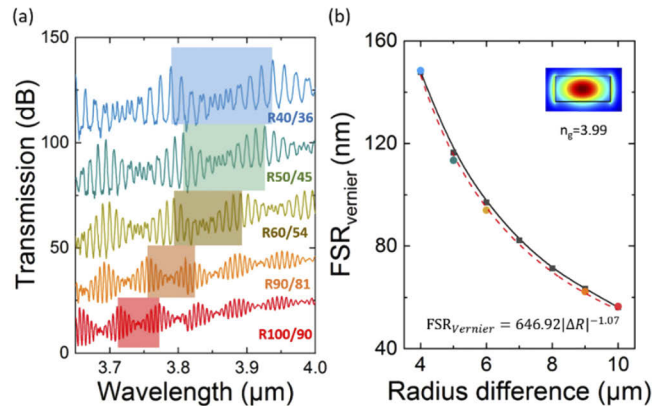


Fig. 3. (a) Spectra of Vernier devices with various radii differences but a fixed coupling gap of 300 nm. The spectra are shifted vertically for clarity. (b) Comparison of theoretical (black line) and measured (red dashed line) results of relationships between FSR_{Vernier} and radius difference. The inset is the TE fundamental mode of the waveguide and the group index is 3.99.

The sub-micron scale coupling gap in ring resonators is generally challenging in fabrication. Therefore, cascaded rings with the fixed radii but varying coupling gaps are fabricated to investigate its fabrication tolerance. Measured spectra of three such designs are plotted in Figs. 4(a)–4(c) for radii of 50/45 μm , 60/54 μm and 90/81 μm respectively, which are referred as R50/45, R60/54 and R90/81. In each figure, spectra are shifted vertically for clarity. The coupling gaps are 300 nm, 350 nm and 400 nm from top to bottom. The center peaks with the highest transmission intensity, together with two interstitial peaks that are besides this center peaks, are selected to evaluate the tolerance by comparing their wavelength. The evaluation results are in Fig. 4(d). The error bars for R50/45 and R60/54 are negligible. The standard deviation for R90/81 is around 4 nm, which is attributed to the small fabrication error in the ring radius. The transmission intensity of the envelope is barely affected by the coupling gap (< 3 dB). In general, the coupling gap shows excellent fabrication tolerance and has a very minor influence on the envelope.

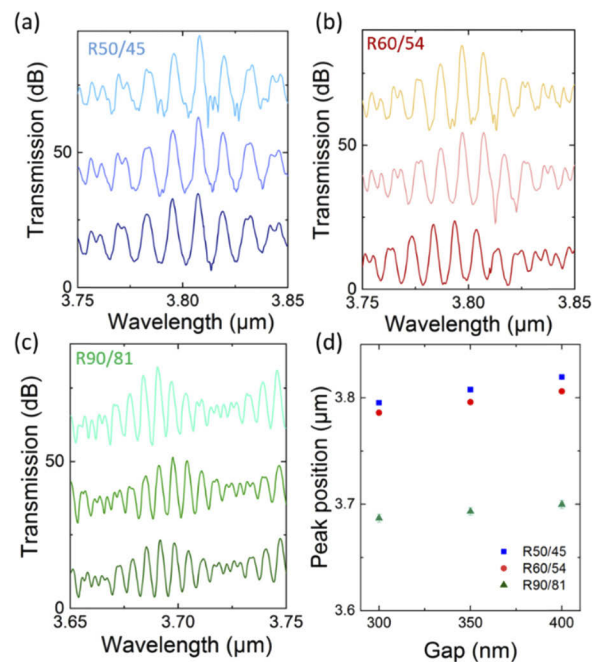


Fig. 4. Measured spectra of cascaded rings with (a) radius 50/45 μm (b) radius 60/54 μm (c) radius 90/81 μm . The coupling gaps are 300 nm, 350 nm and 400 nm from top to bottom. (d) The wavelengths of envelope peaks in three cascaded rings with the same radii but different coupling gaps.

3. Thermal tuning

It is desired that the maximum of the envelope is overlapped with the major absorption fingerprints so that the significant transmission drop in the envelope peak can be observed. However, the imperfections in the fabrication may lead to the variation of the radius and thus the wavelength of the maximum of the envelope. If this occurs, the thermal tuning could compensate for the drift in the fabrication and realign the envelope with the molecular fingerprints. In our devices, TiN heaters are deposited on the reference ring (radius 90 μm) of the previous cascaded rings R90/81. Refractive index of Si is increased when heat is generated by applied currents so that the Vernier envelope redshifts. The spectra under different power are plotted in Fig. 5(a). A

23.2 nm envelope shift from 3.7582 μm to 3.7814 μm is achieved when 232 mW heating power is applied. The sensitivity is determined by linear fitting as shown in Fig. 5(b). The fitted slope indicates a sensitivity of 0.091 nm/mW. The relatively low sensitivity is attributed to the low thermal-optic coefficient of Si ($1.86 \times 10^{-4} / ^\circ\text{C}$) and the weak interaction between generated heat and propagation mode in the resonator. Only around ten percent of the resonator circumference is covered by the TiN electrode and well-overlapped with the thermal field.

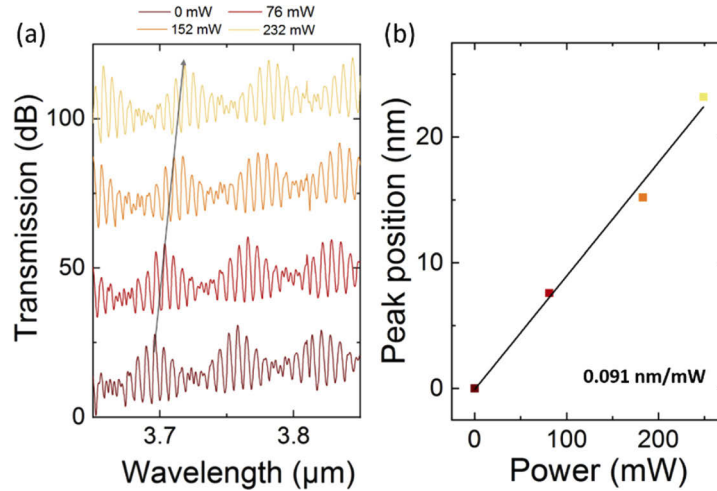


Fig. 5. Measured spectra of cascaded rings R90/81 under different applied power. Spectra are shifted vertically for illustration purposes. The arrow indicates the redshift. (b) Fitting results between the peak redshift and the applied power.

4. Sensing results and discussion

It is expected that Vernier effect-based MIR sensors can leverage both the high sensitivity offered by refractometric sensing and the selectivity offered by absorption sensing. A complex index sensing can be realized in MIR. To experimentally demonstrate this concept, the cladding SiO_2 above the sensing ring, whose radius is smaller, is etched away to precisely define the sensing region. A polydimethylsiloxane (PDMS) microfluidic channel is bonded to the sensor in order to control the liquid flow. Before bonding, the SiO_2 surface is treated by O_2 plasma at 400 mTorr and 30 W for 30 s. The inlet of the microfluidic channel is connected to a syringe pump. We use acetone ($n = 1.35$) and isopropanol (IPA, $n = 1.382$) as analytes in the experiment [39,40].

The measured spectra of cascaded rings R100/90 under different cladding materials are plotted in Fig. 6(a). After the SiO_2 cladding is removed, the group index of the TE mode changes dramatically from 3.99 to 4.19 and the FSR_{Vernier} is enlarged to 90 nm. When the devices are immersed in the acetone, the characteristic envelope is still clear due to the weak absorption of acetone. This weak absorption is also confirmed by the negligible transmission intensity decrease (~ 1 dB), which is the intensity differences at the envelope maximum as highlighted by the circles in Fig. 6(a). The field overlap of the waveguide modes with the acetone is simulated as 15.71%. A mixture of acetone and IPA at a 1:1 ratio ($n = 1.366$) introduces a considerable loss so that the intensity drops by 8 dB. Since the sensing ring has a smaller radius and $FSR_{\text{ref}} < FSR_{\text{sensor}}$, the overall envelopes blueshift by 46 nm [41]. Although the coupled power between the bus waveguide and the sensing ring can be varied by the refractive index of different analytes, such an effect is negligible when considering the minor deviation in the refractive index (0.016 RIU) in our case. The heavy loss from the sensing ring dominates the decrease in transmission

level. When the microfluidic channel is filled by IPA, the strong broadband absorption further decreases the transmission intensity so that the extinction ratio of the envelope is reduced and the Vernier characteristic envelope can barely be recognized. Figure 6(b) is an image of the device under test. The measured Vernier spectra of different devices at different analytes are plotted in Fig. 6(c). The envelope shifts and intensity drops are summarized in Fig. 6(d) for different geometric designs. These three sensors achieve comparable peak shifts around 40 nm because their Vernier gains are close to each other, which mainly depend on the ratio of two ring radii as shown in Eq. (5). Based on the estimated refractive index above, the refractometric sensitivity of R60/54, R90/81 and R100/90 is 3000 nm/RIU, 2575 nm/RIU and 2875 nm/RIU. In refractometric sensing, LOD is equal to the ratio of the $FSR_{interstitial}$ and the sensitivity because the Vernier effect based sensor is a digitized sensor [41]. The refractometric LOD (n_{LOD}) is 0.0033 RIU, 0.00258 RIU and 0.002 RIU for R60/54, R90/81 and R100/90 and corresponding minimum concentrations detectable are calculated as 10.31%, 8.1% and 6.25% of IPA in acetone, using equation $\frac{n_{LOD}}{n_{acetone} - n_{IPA}}$. This refractometric LOD is mainly limited by the $FSR_{interstitial}$, the minimum of which is only 6 nm in the R100/90. If a Vernier device is designed to approach the step limit of our laser (0.1 nm), the minimum concentration detectable can be reduced to less than 1%. It can further be improved by adopting rings with smaller radii differences for a larger Vernier gain. A waveguide design that exposes more fields is also favored.

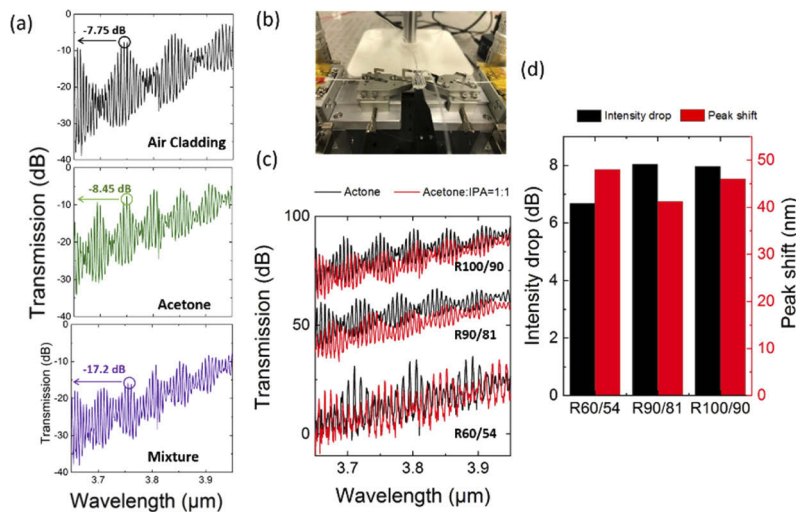


Fig. 6. (a) Measured spectra of cascaded rings R100/90 under different claddings. (b) Image of the device under test: photonic chips bonded with PDMS microfluidic channel and aligned with the input and output butt coupling fiber. (c) Measured Vernier spectra of different devices under acetone (black) and a mixture of acetone and IPA at 1:1 (red). (d) Intensity drop and peak shift of three cascaded rings extracted from (c).

Besides the refractometric sensing, the LOD is characterized again in the absorption sensing, where the noise is decided by the laser power fluctuation and noise equivalent power (NEP) of the photodetector. In our case, the laser power fluctuation is 7%, which is 0.3 dB. Considering the laser to fiber coupling efficiency and the butt coupling efficiency (7.5 dB/facet) in our system [42], the power at the input fiber is 25 mW and the detected power of reference waveguides is 0.8 mW, to which the measured Vernier spectra are normalized. Because the normalized transmission for devices in the acetone-IPA mixture is around -25 dB as shown in Fig. 6(a), the output power is 2.5 μ W and the power fluctuation is \pm 87.5 nW. When comparing this power level to the NEP of our PbSe photodetector (PDA20H, Thorlab) around 1.5×10^{-10} W/Hz^{1/2}, the dominating noise

is the laser power fluctuation. Therefore, the LOD is calculated by $\frac{\Delta T_{overall}}{T_{noise}} \Delta C$, where T_{Noise} is the laser power fluctuation, $\Delta T_{overall}$ is the total transmission drop and ΔC is the corresponding concentration change. Since the transmission drops are 7.96 dB, 8.035 dB and 6.68 dB in the R100/90, R90/81 and R60/54 when the analyte is changed from pure acetone to mixture of acetone and IPA (1:1), the minimum concentrations detectable are 1.88%, 1.87% and 2.25% respectively.

Although the absorption from SiO₂ induces the propagation loss and decreases the quality factor of the ring resonators, our sensor generally works well from 3.65 μm to 3.95 μm. There is no severe deterioration observed because the absorption from SiO₂ in this range is still moderate [22,43]. However, the interstitial peaks inside the Vernier envelope potentially become broader so that the peak shift is less pronounced. Therefore, the refractometric sensitivity and LOD of the sensor may be affected. It is also observed that the extinction ratio of the envelope is gradually reduced when the wavelength is longer than 3.8 μm.

The molecular fingerprints are expected to be resolved in the absorption sensing. In the Vernier based sensors, the resolution is decided by the $FSR_{interstitial}$, which is 6 nm in the R100/90. Although this achieved resolution is one order higher than the typical resolutions (0.11 nm) in the gas phase database [44] and is not suitable to establish a spectroscopic database, it can find its applications in distinguishing and sensing chemical mixtures. If higher resolutions are required, a ring with longer circumference can help to provide a smaller FSR and thus reduce the resolution.

5. Conclusion

In summary, we investigated Vernier effect-based MIR tunable photonic sensor using cascaded rings. Radii and coupling gaps are studied experimentally as the key design parameters. The linear relationship between $FSR_{Vernier}$ and ΔR^{-1} agrees well with the theory and the coupling gap shows excellent fabrication tolerance. Besides, the thermal tunability is realized at a sensitivity of 0.091 nm/mW. In the acetone/IPA sensing, an envelope shift of 48 nm and an intensity drop of 6.7 dB are observed, verifying the feasibility of complex index sensing. The demonstrated refractometric sensitivity is 3000 nm/RIU and LOD is 0.002 RIU, which shows the potential to realize a minimum detectable concentration of less than 1% IPA in acetone. In the absorption sensing, the minimum detectable concentration is 1.87% of IPA in acetone. The high sensitivity offered by the refractometric sensing and the selectivity in absorption sensing can be leveraged simultaneously for mixture sensing in the environment, healthcare, and industrial monitoring applications.

Funding

National Research Foundation Singapore (R-263000C24281, R-263000C64281).

Disclosures

The authors declare no conflicts of interest.

References

1. X. Fan, I. M. White, S. I. Shopova, H. Zhu, J. D. Suter, and Y. Sun, "Sensitive optical biosensors for unlabeled targets: A review," *Anal. Chim. Acta* **620**(1-2), 8–26 (2008).
2. K. De Vos, I. Bartolozzi, E. Schacht, P. Bienstman, and R. Baets, "Silicon-on-Insulator microring resonator for sensitive and label-free biosensing," *Opt. Express* **15**(12), 7610–7615 (2007).
3. B. Schwarz, P. Reininger, D. Ristanić, H. Detz, A. M. Andrews, W. Schrenk, and G. Strasser, "Monolithically integrated mid-infrared lab-on-a-chip using plasmonics and quantum cascade structures," *Nat. Commun.* **5**(1), 4085 (2014).
4. N. N. Klimov, S. Mittal, M. Berger, and Z. Ahmed, "On-chip silicon waveguide Bragg grating photonic temperature sensor," *Opt. Lett.* **40**(17), 3934–3936 (2015).

5. W. Xiang and C. Lee, "Nanophotonics sensor based on microcantilever for chemical analysis," *IEEE J. Sel. Top. Quantum Electron.* **15**(5), 1323–1326 (2009).
6. F.-L. Hsiao and C. Lee, "Computational study of photonic crystals nano-ring resonator for biochemical sensing," *IEEE Sens. J.* **10**(7), 1185–1191 (2010).
7. T. T. Mai, F.-L. Hsiao, C. Lee, W. Xiang, C.-C. Chen, and W. Choi, "Optimization and comparison of photonic crystal resonators for silicon microcantilever sensors," *Sens. Actuators, A* **165**(1), 16–25 (2011).
8. B. Li, F.-L. Hsiao, and C. Lee, "Computational characterization of a photonic crystal cantilever sensor using a hexagonal dual-nanoring-based channel drop filter," *IEEE Trans. Nanotechnol.* **10**(4), 789–796 (2011).
9. C. P. Ho, B. Li, A. J. Danner, and C. Lee, "Design and modeling of 2-D photonic crystals based hexagonal triple-nano-ring resonators as biosensors," *Microsyst. Technol.* **19**(1), 53–60 (2013).
10. D. Dai, "Highly sensitive digital optical sensor based on cascaded high-Q ring-resonators," *Opt. Express* **17**(26), 23817–23822 (2009).
11. Y. Liu, Y. Li, M. Li, and J.-J. He, "High-sensitivity and wide-range optical sensor based on three cascaded ring resonators," *Opt. Express* **25**(2), 972–978 (2017).
12. H. Zhu, Y. Yue, Y. Wang, M. Zhang, L. Shao, J. He, and M. Li, "High-sensitivity optical sensors based on cascaded reflective MZIs and microring resonators," *Opt. Express* **25**(23), 28612–28618 (2017).
13. J. Hu and D. Dai, "Cascaded-ring optical sensor with enhanced sensitivity by using suspended Si-nanowires," *IEEE Photonics Technol. Lett.* **23**(13), 842–844 (2011).
14. X. Jiang, J. Ye, J. Zou, M. Li, and J.-J. He, "Cascaded silicon-on-insulator double-ring sensors operating in high-sensitivity transverse-magnetic mode," *Opt. Lett.* **38**(8), 1349–1351 (2013).
15. Z. Xie, Z. Cao, Y. Liu, Q. Zhang, J. Zou, L. Shao, Y. Wang, J. He, and M. Li, "Highly-sensitive optical biosensor based on equal FSR cascaded microring resonator with intensity interrogation for detection of progesterone molecules," *Opt. Express* **25**(26), 33193–33201 (2017).
16. Y. Chen, W. S. Fegadolli, W. M. Jones, A. Scherer, and M. Li, "Ultrasensitive gas-phase chemical sensing based on functionalized photonic crystal nanobeam cavities," *ACS Nano* **8**(1), 522–527 (2014).
17. J. Haas and B. Mizaikoff, "Advances in mid-infrared spectroscopy for chemical analysis," *Annu. Rev. Anal. Chem.* **9**(1), 45–68 (2016).
18. H. Lin, Z. Luo, T. Gu, L. C. Kimerling, K. Wada, A. Agarwal, and J. Hu, "Mid-infrared integrated photonics on silicon: a perspective," *Nanophotonics* **7**(2), 393–420 (2017).
19. Y. Zou, S. Chakravarty, C.-J. Chung, X. Xu, and R. T. Chen, "Mid-infrared silicon photonic waveguides and devices," *Photonics Res.* **6**(4), 254–276 (2018).
20. J. Wei, Y. Li, Y. Chang, D. M. N. Hasan, B. Dong, Y. Ma, C. Qiu, and C. Lee, "Ultrasensitive Transmissive Infrared Spectroscopy via Loss Engineering of Metallic Nanoantennas for Compact Devices," *ACS applied materials & interfaces* (2019).
21. Y. Chang, D. Hasan, B. Dong, J. Wei, Y. Ma, G. Zhou, K. W. Ang, and C. Lee, "All-dielectric surface-enhanced infrared absorption-based gas sensor using guided resonance," *ACS Appl. Mater. Interfaces* **10**(44), 38272–38279 (2018).
22. T. Hu, B. Dong, X. Luo, T.-Y. Liow, J. Song, C. Lee, and G.-Q. Lo, "Silicon photonic platforms for mid-infrared applications," *Photonics Res.* **5**(5), 417–430 (2017).
23. Y. Ma, B. Dong, B. Li, J. Wei, Y. Chang, C. P. Ho, and C. Lee, "Mid-infrared slow light engineering and tuning in 1-D grating waveguide," *IEEE J. Sel. Top. Quantum Electron.* **24**(6), 1–8 (2018).
24. N. Chen, B. Dong, X. Luo, H. Wang, N. Singh, G.-Q. Lo, and C. Lee, "Efficient and broadband subwavelength grating coupler for 3.7 μm mid-infrared silicon photonics integration," *Opt. Express* **26**(20), 26242–26256 (2018).
25. J. Wei, F. Sun, B. Dong, Y. Ma, Y. Chang, H. Tian, and C. Lee, "Deterministic aperiodic photonic crystal nanobeam supporting adjustable multiple mode-matched resonances," *Opt. Lett.* **43**(21), 5407–5410 (2018).
26. Y. Ma, B. Dong, B. Li, K.-W. Ang, and C. Lee, "Dispersion engineering and thermo-optic tuning in mid-infrared photonic crystal slow light waveguides on silicon-on-insulator," *Opt. Lett.* **43**(22), 5504–5507 (2018).
27. F. Sun, J. Wei, B. Dong, Y. Ma, Y. Chang, H. Tian, and C. Lee, "Coexistence of air and dielectric modes in single nanocavity," *Opt. Express* **27**(10), 14085–14098 (2019).
28. B. Dong, T. Hu, X. Luo, Y. Chang, X. Guo, H. Wang, D.-L. Kwong, G.-Q. Lo, and C. Lee, "Wavelength-Flattened Directional Coupler Based Mid-Infrared Chemical Sensor Using Bragg Wavelength in Subwavelength Grating Structure," *Nanomaterials* **8**(11), 893 (2018).
29. P. T. Lin, V. Singh, J. Hu, K. Richardson, J. D. Musgraves, I. Luzinov, J. Hensley, L. C. Kimerling, and A. Agarwal, "Chip-scale Mid-Infrared chemical sensors using air-clad pedestal silicon waveguides," *Lab Chip* **13**(11), 2161–2166 (2013).
30. Y. Zou, H. Subbaraman, S. Chakravarty, X. Xu, A. Hosseini, W.-C. Lai, P. Wray, and R. T. Chen, "Grating-coupled silicon-on-sapphire integrated slot waveguides operating at mid-infrared wavelengths," *Opt. Lett.* **39**(10), 3070–3073 (2014).
31. Y. Zou, S. Chakravarty, P. Wray, and R. T. Chen, "Mid-infrared holey and slotted photonic crystal waveguides in silicon-on-sapphire for chemical warfare simulant detection," *Sens. Actuators, B* **221**, 1094–1103 (2015).
32. Z. Han, P. Lin, V. Singh, L. Kimerling, J. Hu, K. Richardson, A. Agarwal, and D. Tan, "On-chip mid-infrared gas detection using chalcogenide glass waveguide," *Appl. Phys. Lett.* **108**(14), 141106 (2016).

33. V. M. Passaro, B. Troia, and F. De Leonardis, "A generalized approach for design of photonic gas sensors based on Vernier-effect in mid-IR," *Sens. Actuators, B* **168**, 402–420 (2012).
34. C. P. Ho, Z. Zhao, Q. Li, S. Takagi, and M. Takenaka, "Mid-infrared tunable Vernier filter on a germanium-on-insulator photonic platform," *Opt. Lett.* **44**(11), 2779–2782 (2019).
35. B. Troia, A. Z. Khokhar, M. Nedeljkovic, J. S. Penades, V. M. Passaro, and G. Z. Mashanovich, "Cascade-coupled racetrack resonators based on the Vernier effect in the mid-infrared," *Opt. Express* **22**(20), 23990–24003 (2014).
36. S. Radosavljevic, N. T. Beneitez, A. Katumba, M. Muneeb, M. Vanslembrouck, B. Kuyken, and G. Roelkens, "Mid-infrared Vernier racetrack resonator tunable filter implemented on a germanium on SOI waveguide platform," *Opt. Mater. Express* **8**(4), 824–835 (2018).
37. B. Troia, J. S. Penades, A. Z. Khokhar, M. Nedeljkovic, C. Alonso-Ramos, V. M. Passaro, and G. Z. Mashanovich, "Germanium-on-silicon Vernier-effect photonic microcavities for the mid-infrared," *Opt. Lett.* **41**(3), 610–613 (2016).
38. W. Bogaerts, P. De Heyn, T. Van Vaerenbergh, K. De Vos, S. Kumar Selvaraja, T. Claes, P. Dumon, P. Bienstman, D. Van Thourhout, and R. Baets, "Silicon microring resonators," *Laser Photonics Rev.* **6**(1), 47–73 (2012).
39. E. Sani and A. Dell'Oro, "Spectral optical constants of ethanol and isopropanol from ultraviolet to far infrared," *Opt. Mater.* **60**, 137–141 (2016).
40. J. Rheims, J. Köser, and T. Wriedt, "Refractive-index measurements in the near-IR using an Abbe refractometer," *Meas. Sci. Technol.* **8**(6), 601–605 (1997).
41. T. Claes, W. Bogaerts, and P. Bienstman, "Experimental characterization of a silicon photonic biosensor consisting of two cascaded ring resonators based on the Vernier-effect and introduction of a curve fitting method for an improved detection limit," *Opt. Express* **18**(22), 22747–22761 (2010).
42. B. Dong, X. Guo, C. P. Ho, B. Li, H. Wang, C. Lee, X. Luo, and G.-Q. Lo, "Silicon-on-insulator waveguide devices for broadband mid-infrared photonics," *IEEE Photonics J.* **9**(3), 1–10 (2017).
43. J. S. Penadés, C. Alonso-Ramos, A. Khokhar, M. Nedeljkovic, L. Boodhoo, A. Ortega-Moñux, I. Molina-Fernández, P. Cheben, and G. Mashanovich, "Suspended SOI waveguide with sub-wavelength grating cladding for mid-infrared," *Opt. Lett.* **39**(19), 5661–5664 (2014).
44. S. W. Sharpe, T. J. Johnson, R. L. Sams, P. M. Chu, G. C. Rhoderick, and P. A. Johnson, "Gas-phase databases for quantitative infrared spectroscopy," *Appl. Spectrosc.* **58**(12), 1452–1461 (2004).